Fuel 388 (2025) 134413

Contents lists available at ScienceDirect

Fuel

journal homepage: www.elsevier.com/locate/fuel

Full Length Article

Comparison of steam and dry reforming adsorption kinetics in solid oxide fuel cells

Saeed Moarrefi [a], Mohan Jacob [a], Nilay Shah [b], Stephen Skinner [c], Weiwei Cai [d,e,f], Liyuan Fan [a,*]

[a] College of Science and Engineering, James Cook University, 1 James Cook Drive, Townsville QLD 4811, Australia
[b] Department of Chemical Engineering, Imperial College London, London, UK
[c] Department of Materials, Imperial College London, London, UK
[d] Hydrogen Energy Technology Innovation Center of Hubei Province, Faculty of Materials Science and Chemistry, China
[e] University of Geosciences, Wuhan, 430074, Hubei, China
[f] Faculty of Materials Science and Engineering, Kunming University of Science and Technology, Kunming 650093, China

ARTICLE INFO

Keywords:
Dry Reforming Kinetics
Langmuir–Hinshelwood SOFC
Steam Reforming Kinetics
Power-Law

ABSTRACT

Internal steam reforming (SRM) and dry reforming of methane (DRM) within solid oxide fuel cells offer significant potential for zero-carbon energy production. This study explores how electrochemical reactions influence reforming kinetics, which is crucial for designing fuel cell materials under various conditions. The research examines how gas composition, process temperature, and current draw from the fuel cell impact methane reforming adsorption kinetics.

Both processes inside solid oxide fuel cells have been studied individually under varying conditions and anode materials, leaving a significant research gap in understanding electrochemical interactions' impact on catalytic behavior within a unified fuel cell framework. Findings indicate that increasing methane-to- H_2O and CO_2 ratio decreases methane conversion. Both processes show higher methane conversion with increased current density drawn from the fuel cell. In comparison, SRM achieves greater methane conversion than DRM under equal methane concentration in the feed stream. SRM also produces more hydrogen than DRM inside the fuel cell. Reforming reaction rates increase with fuel cell temperature, and DRM consumes methane slower than SRM. Higher methane concentration in the feed and current density boost reaction rates. The reaction order for H_2O is generally higher than CO_2 in Langmuir–Hinshelwood model but lower than CH_4. Both processes show reduced activation energy when current is drawn, with current density affecting H_2O adsorption enthalpy more than CO_2. The SRM model estimates activation energy more accurately, while the DRM model has an R^2 value close to 0.95, indicating acceptable accuracy.

1. Introduction

The Paris Agreement of 2015, adopted by 196 nations globally, is a collective effort to address climate change[1]. Its primary objectives are to prevent substantial global warming by restricting the temperature increase to less than 2 °C from preindustrial levels, with an additional ambition to limit it to 1.5 °C. Achieving these objectives necessitates reducing greenhouse gas emissions by 2025 and a subsequent reduction of 43 % by 2030 [2,3]. The agreement also facilitates countries in handling the effects of climate change and supports them in finding possible solutions for mitigating carbon emissions to the atmosphere[4]. Solid Oxide Fuel Cells (SOFCs) play an important role in reducing carbon emissions to the ecosystem by offering a cleaner and more efficient alternative for power generation. Their ability to utilize various fuels, capture and utilize carbon, and integrate with renewable energy sources positions them as a sustainable technology for the future [5,6].

The syngas, a mixture of H_2 and CO, with electricity, can be simultaneously generated in SOFCs by steam reforming of methane (SRM) or dry reforming of methane (DRM) [7]. In the DRM, biogas containing CH_4, and CO_2 react at elevated temperatures to convert into syngas, as represented by reaction (1). Following the sequence, a reverse water gas shift reaction (RWGS) occurs, as described in reaction (2).

$$CH_4 + CO_2 \rightarrow 2CO + 2H_2 \qquad \Delta H^{\circ}_{298} = +247\,\mathrm{kJ\,mol^{-1}},\ \mathrm{DRM} \tag{1}$$

$$CO_2 + H_2 \rightarrow CO + H_2O\,(g) \qquad \Delta H^{\circ}_{298} = +41\,\mathrm{kJ\,mol^{-1}},\ \mathrm{RWGS} \tag{2}$$

---

* Corresponding author.
E-mail address: liyuan.fan@jcu.edu.au (L. Fan).

https://doi.org/10.1016/j.fuel.2025.134413
Received 22 September 2024; Received in revised form 5 January 2025; Accepted 14 January 2025

Nomenclature

Abbreviations

DRM	Dry Reforming of Methane
DIR	Direct Internal Reforming
LH	Langmuir-Hinshelwood
RWGS	Reverse Water Gas Shift
SOFC	Solid Oxide Fuel Cell
NiO-YSZ	Nickel-Yttria-Stabilized-Zirconia
NiO-GDC	Nickel-Gadolinium-Doped-Ceria
PL	Power Law
RDS	Rate Determining Step
R_{SRM}	Methane Ratio to Steam
R_{DRM}	Methane Ratio to Carbon Dioxide
SRM	Steam Reforming of Methane
TPB	Triple-phase boundary
WGS	Water Gas Shift
SEFAC	surface electric field-assisted catalysis
RMSE	Root Mean Square Error
OCV	Open Circuit Voltage

Latin symbols

P	Constant total pressure, 1 bar
R	Universal gas constant
r	Reaction rate
T	Temperature, K
k	Rate constant
a	Reaction order of methane
b	Reaction order of carbon dioxide or steam
R^2	R-squared

Subscripts

x_{CH_4}	Overall methane conversion
$F_{CH_4}^{inlet}$	Methane flow rate at the inlet, ml/min
$F_{CH_4}^{outlet}$	Methane flow rate at the outlet, ml/min
W_{cat}	Total weight of the catalyst, g
r_{CH_4}	Reaction rate of methane, mol/s/g
k_0	The pre-exponential factor of rate constant, mol/ (s g $bar^{(a+b)}$)
p_j	The partial pressure of species j, bar
K_j	Adsorption equilibrium constant of species j, bar^{-1}
A_j	The pre-exponential factor of the adsorption constant of species j
ΔH_j	The change of adsorption enthalpy of species j, kJ/mol
ΔS_j	The change of adsorption entropy of species j, J/mol.K
ΔG_j	The Change of Gibbs free energy of adsorption for species j, kJ/mol
K_{eq}	Equilibrium constant of DRM
K_{RWGS}	Equilibrium constant of RWGS
K_{WGS}	Equilibrium constant of WGS
df	Driving force
E_a	Activation energy, kJ/mol

On the other hand, in the SRM, CH_4 reacts with steam (H_2O) to yield syngas, as depicted by reaction (3). The water gas shift (WGS) reaction occurs sequentially, leading to an enhanced H_2 yield, as described in reaction (4).

$$CH_4 + H_2O\,(g) \rightarrow CO + 3H_2 \qquad \Delta H^{\circ}_{298} = +206\,kJ\,mol^{-1},\ SRM \tag{3}$$

$$H_2O\,(g) + CO \rightarrow CO_2 + H_2 \qquad \Delta H^{\circ}_{298} = -41\,kJ\,mol^{-1},\ WGS \tag{4}$$

Carbon deposition may arise from either a methane cracking reaction (5) or the Boudouard reaction (6), resulting in solid carbon on the anode surface and impacting hydrogen and electricity generation.

$$CH_4 \rightarrow C(s) + 2H_2 \qquad \Delta H^{\circ}_{298} = +75\,kJ\,mol^{-1},\ Methane\ Cracking \tag{5}$$

$$2CO \leftrightarrow C(s) + CO_2 \qquad \Delta H^{\circ}_{298} = -171\,kJ\,mol^{-1},\ Boudouard \tag{6}$$

SRM is known for its higher H_2 yield, and more energy efficiency as it operates at lower temperatures [8], with a lower risk of carbon deposition[9]. On the other hand, DRM offers potential for carbon capture and utilization by directly converting CO_2 into valuable syngas, thereby reducing the overall carbon footprint [9–11]. The endothermic reforming reaction helps balance the thermal profile within the SOFC, potentially mitigating thermal stresses associated with the exothermic nature of SRM when combined with electrochemical reactions[12]. Furthermore, DRM eliminates the need for external water supply and steam generation equipment, simplifying system design and reducing operational costs. Table 1 displays a comparative analysis of DRM and SRM used for methane conversion to energy.

In SOFC technology, two main methods are used: internal and external reforming [17]. Internal reforming directly converts methane into hydrogen within the fuel cell's anode. This approach simplifies the system design and improves thermal efficiency by harnessing the heat generated during the reaction. However, it faces challenges like managing reaction rates and carbon deposition.[5,17]. Conversely, external reforming occurs in a separate unit where CH_4 is reformed into H_2 before being supplied to the fuel cell. This method offers better control over the reforming process and improves H_2 purification but introduces added system complexity and cost[7,17–21]. The electrochemical reactions over the SOFC anode include hydrogen oxidation to protons (H^+) and electrons (e^-), which generate electrical power. When methane is used as a fuel, it undergoes DRM or SRM, producing hydrogen and carbon monoxide. Additionally, carbon monoxide can be electrochemically oxidized to carbon dioxide at the anode. The electrochemical activity at the anode influences the reforming kinetics of DRM and SRM by affecting reaction rates, local temperature, and the concentration of reactants. The generation of oxide ions (O^{2-}) and electrons at the anode can facilitate or hinder these reforming reactions, impacting fuel

Table 1
Comparative analysis of methane dry reforming vs. steam reforming for methane conversion[4,8–10,13–16].

Aspect	DRM	SRM
Reaction Type	Endothermic	Endothermic
Temperature Requirements	Operates at higher temperatures	Operates at relatively lower temperatures
Process rate	Low	High
Fuel Conversion Efficiency	30 – 45	85 – 95
Carbon Formation Risk	Higher	Lower
Thermodynamic Considerations	Higher heat input	Lower heat input
Operating Costs	higher operating costs	lower operating costs
Greenhouse Gas Emissions	Directly reducing CO_2 emissions	Doesn't directly reduce CO_2 emissions
Energy Efficiency	Less energy-efficient	More energy-efficient
CO2 content in products	Lower	Higher
Environmental Impact	Lower with no water required	Higher with direct water consumption
Feasibility and Complexity	Less complex	More complex

conversion efficiency and hydrogen production. Understanding these coupled electrochemical and thermochemical processes is crucial because it helps optimize SOFC performance. However, carbon deposition and the agglomeration of metal nanoparticles are common issues during methane reforming on Ni-based catalysts, and these can be effectively minimized by adjusting the SOFC structure[16].

In recent years, extensive research has been conducted on DRM and SRM utilizing various perovskite-based anode materials for internal methane reforming[22–25]. These studies focused primarily on examining the properties of two widely used anode structures: Ni-GDC (Nickel-Gadolinium Doped Ceria)[23,26–28] and Ni-YSZ (Nickel-Yttria Stabilized Zirconia)[29,30]. Bian et al.[31] finding these materials to be both practical and economical for internal reforming, but further research on their kinetic parameters was called for due to their ability to balance electronic conductivity, sulfur, and coking resistance. Literature evidence indicates that applying an electric field through the Surface Electric Field-Assisted Catalysis (SEFAC) approach nearly suppresses coke formation related to the kinetics of adsorption and desorption of reaction species[15]. Besides material investigations, extensive research on process conditions has been done to find suitable methane-to-steam ratios (R_{SRM}) or methane-to-carbon dioxide ratios (R_{DRM}) to ensure efficient operational conditions for both processes[32]. Developing efficient anode materials, alongside simulation studies, requires determining kinetic parameters, understanding adsorption mechanisms, and assessing activation energies.

In the study of reaction mechanisms, several kinetic models are commonly used, including the Power-Law (PL), Langmuir-Hinshelwood (LH), Eley-Rideal (ER), and Mars-van Krevelen (MvK) models[33]. The PL model is a simple, empirical approach that relates reaction rates directly to reactant concentrations, making it useful for identifying general trends in experimental data. In contrast, the LH model focuses on surface-catalyzed reactions, accounting for adsorption, desorption, and surface interactions, which are crucial for understanding the kinetics of DRM and SRM processes[34]. While the ER model is used for reactions involving adsorbed and gas-phase reactants, and the MvK model is applied to catalytic oxidation on metal oxides, the PL and LH models are preferred due to their complementary strengths. The PL model provides a simple analysis of reaction rate trends, while the LH model offers detailed insights into surface mechanisms, allowing for a more comprehensive understanding of complex catalytic systems. This combination of simplicity and mechanistic detail makes the PL and LH models particularly effective for analyzing the kinetics in SOFC applications [22,35–37]. These models aid in understanding how the amounts of CH_4, oxidants (CO_2 and H_2O) and other process variables affect the kinetic parameters, which are crucial for optimizing anode material in SOFCs[25].

Thattai et al. [26] investigated the kinetics of SRM within Ni-GDC anodes to suggest universal models to understand the effects of electrochemical interactions on kinetic parameters inside SOFCs. By comparing two types of rate expressions, PL and LH, their research uncovers limitations in existing models, pointing out the necessity for more research on perovskite-based anode materials under the influence of current. Fan et al.[23] reported that the current density had a positive impact, and steam negatively affected the overall SRM reaction rate on a Ni-GDC anode. They also conducted another kinetic study [35] using Ni-YSZ anodes and reported that the electrochemical reactions positively affected the overall SRM reaction rate on the anode. However, the steam adsorption constant over the Ni-YSZ anode was found to be affected differently by changes in current density. These observations encouraged Zhou et al. [32] to conduct another study to determine the adsorption kinetic parameters on Ni-GDC anodes, aiming to underscore the influence of electrochemical interactions on the adsorption of fuel molecules on anode materials used in SOFCs. Besides proposed reaction orders for CH_4 and H_2O components, their model provided a more accurate description of adsorption equilibrium constants, change of adsorption enthalpy and entropy, and activation energy. They also concluded that, for both PL and LH models, the reaction orders were restricted within the range of 0.1 to 1.5 for methane and −0.2 to 1 for steam. However, they noted the relative inaccuracy of the proposed LH model, potentially attributed to its exclusive focus on steam adsorption, leading to discrepancies in the model's predictions. The catalytic internal methane reforming process is intricate, and the performance is heavily influenced by operational conditions. A comprehensive expression for DRM and SRM reforming rates has yet to be established. Wojcik et al. [38] recently reviewed mathematical models for SRM in the temperature range between 773 K and 1273 K, with NiO/YSZ catalysts. The kinetic models presented in that study seem accurate in a broader range of R_{SRM} ratios and can be applied to investigating various kinetic parameters. It is worth noting that their study showed that the complexity of equations doesn't consistently lead to more precise results. However, they reported various reaction orders, activation energies, adsorption constants, and other kinetic parameters, which are particularly related to SRM inside SOFCs (SRM-SOFC). Nevertheless, most studies focused on SRM processes separately from DRM, resulting in the absence of kinetic parameters and rate expressions for internal DRM inside SOFCs (DRM-SOFC). Recent studies using planar SOFCs with large areas (~81 cm2) and catalyst weights over 1 g encountered heat and mass transfer limitations, impacting kinetic data accuracy. Following the recommendations of the International Confederation for Thermal Analysis and Calorimetry (ICTAC) Kinetics Committee, using catalyst weights below 1 g minimizes transport effects[39]. This ensures uniform conditions and measurable reaction rates by reducing transfer limitations with a well-mixed reactor. To address the research gap, a recent study [40] explored the effects of process parameters on DRM-SOFCs using a mixed NiO-GDC and NiO-YSZ (NiO-GDC-YSZ) anode with geometric area of 0.95 cm^2 and catalyst weight below 1. The findings showed that increasing CO_2 concentration improves CH_4 conversion in DRM, driven by the favorable thermodynamics of CO_2 adsorption. Additionally, higher temperatures increased reaction rates by facilitating methane bond division and carbon deposit removal.

It is worth noting that there is still no agreement on the global kinetic model for direct internal methane reforming in the SOFC. This paper aims to address the following research gaps:

1. Most studies focus on SRM kinetics due to its favorable conditions for methane reforming, higher hydrogen production, and lower risk of carbon deposition, which enhances fuel cell performance. There is a lack of comprehensive research on DRM, primarily due to concerns about carbon deposition on the anode side, despite its potential for reducing carbon emissions and offering environmental benefits.
2. DRM and SRM-SOFC systems have been studied separately under varying conditions and with different anode materials, leading to inconsistent reaction orders and kinetic parameters. This highlights the need for a unified investigation into electrochemical interactions within a single SOFC structure.
3. Simulation studies often neglect the effects of current density on the reaction rate, with the Arrhenius equation for methane reforming typically considering only temperature-dependent, which limits the accuracy of simulations.
4. There is a need for a concurrent investigation to identify adsorption kinetic parameters, particularly regarding the competition between oxidants and CH_4 molecules for active sites on catalysts.

This study focuses on the effects of electrochemical reactions on reforming kinetics over a NiO-GDC-YSZ anode in DRM/SRM-SOFC systems. The main novelty lies in analyzing DRM and SRM processes within a single SOFC structure, addressing inconsistencies in previous studies and providing unified, reliable insights into their kinetics.

2. Experiment

2.1. Electrolyte-supported solid oxide fuel cell

This study’s experimental setup and materials were similar to those in our previous study[40]. The experiments began with an electrolyte-supported SOFC (NextCell™), featuring an anode with a geometric area of 0.95 cm^2 and a thickness of 50 µm. The anode NiO-YSZ layer, made up of 66 wt% NiO and 34 wt% $(Y_2O_3)_{0.08}(ZrO_2)_{0.92}$, provides strong catalytic activity for hydrogen oxidation and hydrocarbon reforming, along with good electrical conductivity and thermal expansion compatibility. The NiO-GDC layer with 60 wt% NiO and 40 wt% $(Gd_{0.1}Ce_{0.9})O_{1.95}$ improves hydrocarbon fuel oxidation and offers better resistance to carbon deposition. Together, these layers form a multi-layered anode structure that combines the stability of YSZ with the enhanced catalytic activity of GDC, achieving a synergistic effect. Furthermore, NiO reduces to metallic Ni, a catalyst for key reactions like SRM, DRM, and hydrogen oxidation. Combined with YSZ and GDC, it forms a composite with balanced ionic and electronic conductivity and thermal compatibility. Electrical leakage in electrolyte-supported cells, caused by electrolyte defects or GDC’s electronic conductivity, can reduce efficiency. Using high-purity YSZ and optimizing sintering and microstructure minimizes leakage and enhances ionic conductivity. This design is also expected to last longer than traditional NiO-YSZ anodes.

Fig. 1(a) illustrates the experimental setup. Gases are supplied from cylinders (1) and directed through ½-inch stainless steel tubing to a gas control panel (2). Pressure regulators with a ½-inch orifice diameter ensure consistent gas pressure, while mass flow controllers (Bronkhorst Thermo™) with a ¼-inch orifice diameter, connected to a PC (10), precisely regulate gas flow rates for accurate fuel delivery. The fuel mixture passes through a humidifier (3), a 250 mL conical flask, which removes impurities and adds approximately 2 wt% humidity at ambient temperature, enhancing the fuel quality for the fuel cell. The gas is fed directly to the fuel cell’s anode in the DRM process. For SRM, a syringe pump (4) (Model NE-1000 Multi-Phaser™) injects water into the line, which is electrically heat-traced at 400 K to generate steam. The fuel mixture is directed through an internal tube within an alumina housing (details in Fig. 1(b)) designed to attach to the SOFC, where it enters the fuel inlet channel. The outer tube carries the off-gas from the anode to a condenser. A tube furnace (5), specifically designed for fuel cell applications, maintains the required reaction temperature. By-products like water are collected in a condenser (6), a 250 mL conical flask. A silica gel moisture absorber (7) then dries the anode off-gas before analysis. Gas composition, particularly methane concentration, is analyzed using a gas chromatograph (Shimadzu Nexis GC-2030) (8) to support kinetic studies. Throughout the experiment, an electrochemical test station (Metrohm Autolab PGSTAT302N) (9) applies defined current densities, measures electrical loads, and records data to evaluate cell performance and electrochemical behavior.

Fig. 1(b) illustrates the fuel cell setup, where the fuel gas stream is directed through an alumina tube to the anode side. Fig. 1(c) and Fig. 1(d) show the functional layers of the SOFC and the associated reforming reactions. The anode (NiO-GDC-YSZ) facilitates fuel oxidation, while the cathode (LSM/LSM-GDC) supports oxygen reduction. The Hionic™ scandium-stabilized zirconia electrolyte ensures oxygen ion conduction between the anode and cathode, maintaining ionic conductivity at high temperatures. Silver wires (Sigma-Aldrich) serve as current collectors, enabling electron flow between the electrodes and the external circuit. To ensure mechanical stability and prevent leaks during operation, Aremco Ceramabond™ 552 ceramic adhesive is used to bond and seal the components.

2.2. Testing procedure

The fuel cell cathode side was exposed to air in this study, ensuring minimal oxygen depletion. The experiment commenced with a controlled heating process, raising the furnace temperature by 2 K/min under a nitrogen flow to the fuel cell, until the target temperature of 1073 K was achieved. Subsequently, a constant flow of saturated hydrogen with water, was implemented to reduce anode and activate the fuel cell. Precise control of flow rates was achieved using mass flow controllers, maintaining a overall flow rate of 8 ml/min (at $T = 273$ K

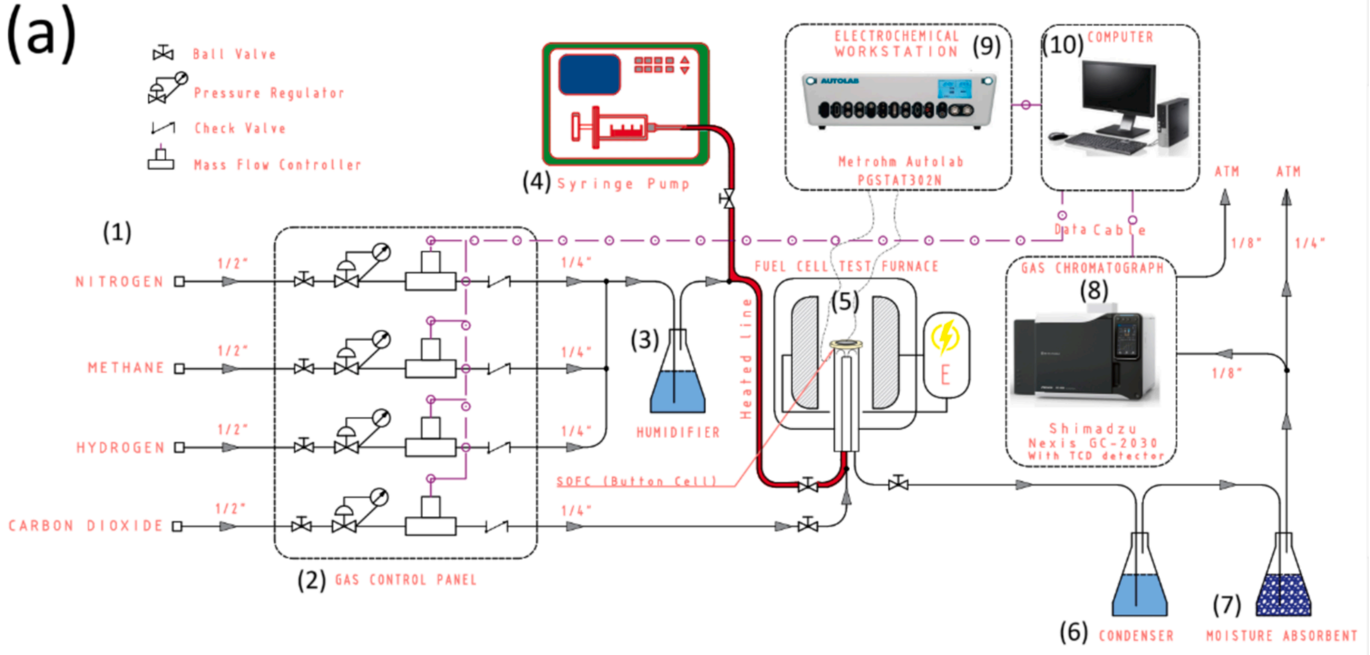

Fig. 1. (a) Experimental setup, including the tube furnace, fuel cell, gas chromatography, mass flow controllers, electrochemical test station, and fuel gas control systems. (b) Schematic of the SOFC device with an anode, cathode and electrolyte layers bonded to an alumina tube using ceramic adhesive. (c) and (d) SOFC structure showing the NiO-GDC-YSZ anode, LSM/LSM-GDC cathode, and Hionic™ scandium-stabilized zirconia electrolyte[41] and main reactions inside the fuel cell. Parts of the figure were adapted from S. Moarrefi et al. [40] reproduced with permission. Copyright 2024, Elsevier.

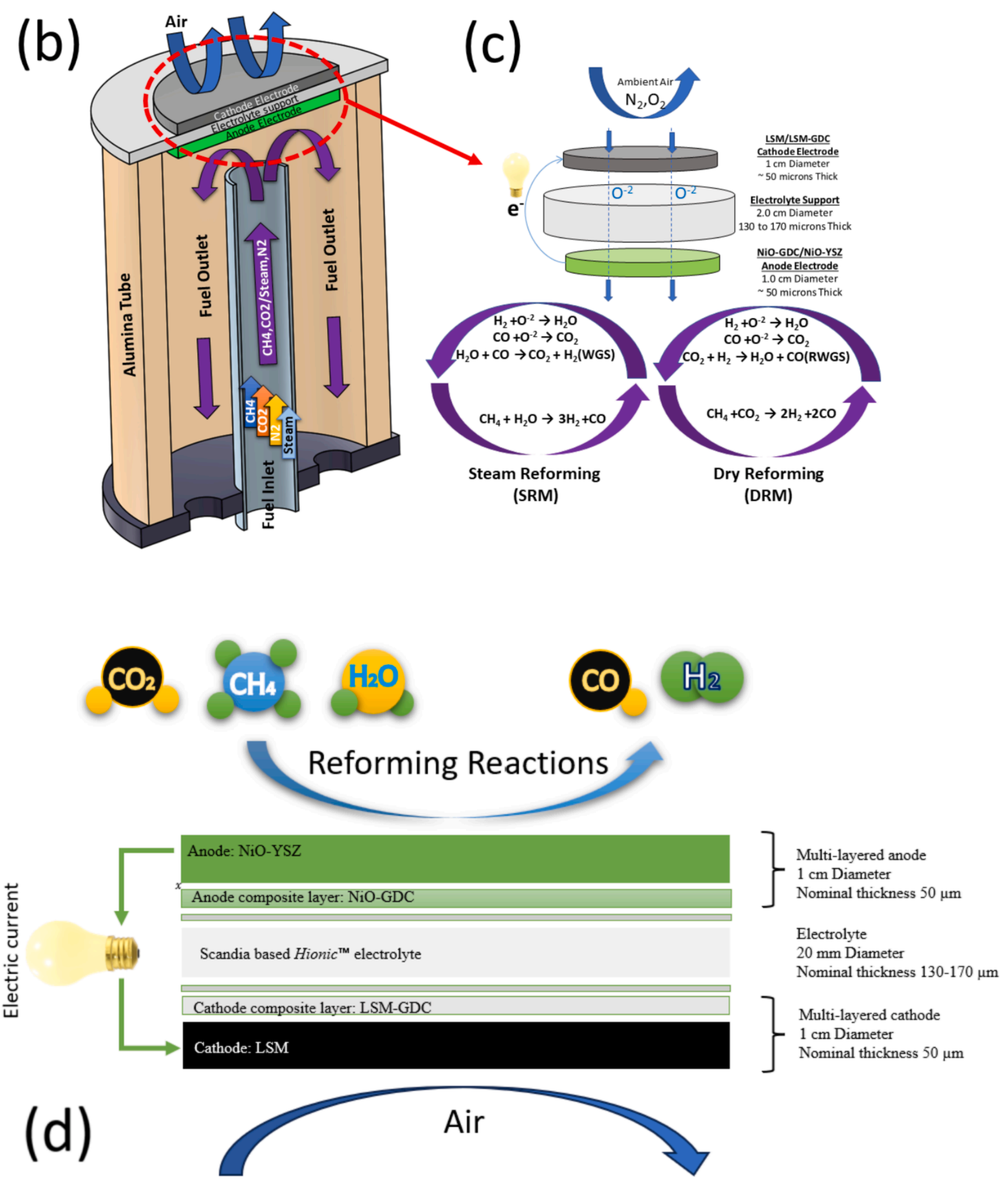

Fig. 1. (*continued*).

and $P = 1$ bar). This experiment examined five specific gas compositions at three temperature set points from 973 K to 1073 K for each process, detailed in Table 2.

Carbon deposition on SOFC anodes occurs when carbon forms as a solid phase, typically as a result of methane reforming or methane cracking at high temperatures. This deposition can block anode active sites, reducing catalytic activity and leading to potential cell failure. Calculations are performed using FactSage™ Education 8.3 software to estimate carbon deposition. The software calculates the equilibrium compositions of reactants and products, including the stability of solid carbon (C(s)), based on the temperature, pressure, and fuel composition. By analyzing the predicted mole fractions of carbon species, FactSage™ helps identify conditions that favor or suppress carbon deposition, providing valuable insights for optimizing SOFC operation and

Table 2
Various inlet gas compositions under standard conditions.

	Case No.	Composition (%)				Carbon Deposition (mol C(s)/min)		
		CH_4	CO_2	N_2	R_{DRM}	T = 973 K	T = 1023 K	T = 1073 K
DRM	i	30	60	10	0.5	0.01	–	–
	ii	30	40	30	0.75	0.04	0.008	–
	iii	40	40	20	1	0.062	0.035	0.016
	iv	50	40	10	1.25	0.078	0.055	0.039
	v	50	33.3	16.7	1.5	0.088	0.069	0.055
SRM		CH_4	H_2O	N_2	R_{SRM}	T = 973 K	T = 1023 K	T = 1073 K
	vi	30	60	10	0.5	–	–	–
	vii	30	40	30	0.75	–	–	–
	viii	40	40	20	1	0.016	0.008	0.002
	ix	50	40	10	1.25	0.037	0.031	0.027
	x	50	33.3	16.7	1.5	0.052	0.048	0.046

minimizing carbon-related issues.

2.3. DRM process

In the DRM-SOFC process, different compositions, methane-rich and methane-poor biogases, are represented by altering the ratio of methane to carbon dioxide (R_{DRM}), which varies from 0.5 to 1.5. Carbon deposition was expected for gas compositions ii, iii, iv, and v, with R_{DRM} ranging from 0.75 to 1.5. These estimations were based on equilibrium calculations performed using FactSage™ Education 8.3 software.

2.4. SRM process

In the SRM-SOFC process, different compositions are represented by altering the methane-to-steam ratio (R_{SRM}), which varies from 0.5 to 1.5. Consequently, deionized water was introduced into the heated line to generate steam. The heated line was adjusted to 130 °C to ensure the water molecules remained in the gaseous phase. In this process, carbon deposition was anticipated for gas compositions viii, ix, and x, according to thermodynamic calculations. The methane composition remained constant in both processes, while the oxidant component varied to investigate their reaction kinetics parameters. At three designated temperatures 973 K, 1023 K, and 1073 K, current densities of open circuit, 500, and 1000 A/m^2 were applied using a galvanostatic method with an Autolab/PGSTAT302N device. To ensure all moisture in the outlet stream was effectively removed, the anode off-gas was subjected to drying through a silica gel moisture removal bed. The resulting outlet gas was analyzed using a Gas Chromatograph (Nexis GC-2030) with a thermal conductivity detector (TCD). The experiment setup is depicted in Fig. 1(c).

3. Methodology

The primary objective of this study is to investigate the kinetics parameters of DRM and SRM on NiO-GDC-YSZ anode material using surface reaction models like PL and more comprehensive models such as LH [42]. The experiment design uses the Van't Hoff equation and Arrhenius expression to conduct experiments within a controlled range of operating temperature and current density of SOFC. The equilibrium constant is determined from the concentrations of reactants and products measured by gas chromatography, and its dependence on temperature and current density is analyzed to calculate enthalpy and entropy changes. Reaction rates are measured to evaluate the rate constant, plotted against temperature in an Arrhenius plot to determine the activation energy and pre-exponential factor [35,40]. In this study, methane conversions were measured at various gas compositions, current densities, and temperatures (see Table 3), and data were fitted to LH and PL kinetics models. Fuel cell voltage ranged from 0.92 V to 0.6 V depending on current density, which is optimal for SOFC kinetics study. Measurements were taken after stable conditions were reached, typically 18 h for DRM and 24 h for SRM, to ensure consistency in current density, cell temperature and gas composition. The overall methane conversion at the anode outlet was calculated using Eq. (7):

$$x_{CH_4} = \frac{F_{CH_4}^{inlet} - F_{CH_4}^{outlet}}{F_{CH_4}^{inlet}} \tag{7}$$

Where $F_{CH_4}^{inlet}$ and $F_{CH_4}^{outlet}$ denote the flow rates of CH_4 (ml/min) at the inlet and outlet, respectively. Table 3 contains methane conversion as a fraction between 0 and 1, observed under different operational conditions calculated using Eq. (1). Based on the GC measurements, conversion values are reported to three decimal places, with an uncertainty of approximately ± 2 % for CH_4 mole fraction measurements.

To investigate the catalytic reaction kinetics within SOFCs, the rate constants and reaction orders are derived by adjusting the models to match the observed data. At the same time, the activation energies and adsorption equilibrium constants are determined by analysing the specific reaction rate at various operating conditions, utilizing the Arrhenius equation. Table 4 presented rate expressions for the PL and LH kinetic models in this study. More details about the proposed models are available in the supplementary material.

where r is the reaction rate, k is the rate constant, and p_{gas} is the partial pressure of the reactants in the mixture. The adsorption constant K_{ads} is a parameter used in surface chemistry to quantify the strength of the interaction between a reactant or any adsorbate and the surface of a catalyst or adsorbent material. In the investigation of methane reforming kinetics, 'a' signifies the CH_4 reaction order, while 'b' represents the CO_2 reaction order in DRM and H_2O in SRM within their respective rate equations. These parameters illustrate how changes in reactant concentrations affect the rate of reaction. In PL, the rate constant 'k' is determined by optimizing 'a' and 'b'. Conversely, in LH, 'k' calculating by optimizing 'a', 'b', the CH_4 adsorption coefficient K_{CH_4}, and the CO_2

Table 3
Methane conversion analysis across operational conditions and current densities for DRM and SRM processes.

		Methane Conversion (Fraction)									
		DRM					SRM				
Temperature [K]	Current Density [A/m2]	i	ii	iii	iv	v	vi	vii	viii	ix	x
973	0	0.174	0.161	0.139	0.128	0.127	0.187	0.188	0.179	0.168	0.147
	500	0.189	0.177	0.150	0.142	0.136	0.197	0.199	0.192	0.180	0.162
	1000	0.213	0.201	0.174	0.158	0.154	0.205	0.206	0.199	0.185	0.168
1023	0	0.209	0.193	0.171	0.161	0.161	0.229	0.230	0.218	0.204	0.178
	500	0.219	0.209	0.182	0.179	0.171	0.231	0.232	0.225	0.212	0.194
	1000	0.245	0.234	0.206	0.190	0.188	0.242	0.242	0.235	0.219	0.202
1073	0	0.219	0.206	0.184	0.173	0.172	0.286	0.280	0.272	0.256	0.224
	500	0.234	0.222	0.195	0.187	0.181	0.286	0.284	0.276	0.261	0.242
	1000	0.258	0.246	0.219	0.203	0.199	0.297	0.297	0.289	0.270	0.253

Table 4

Rate expressions and constants for selected kinetic models[32,43].

Model	Rate Expression		Rate Constant
	DRM	SRM	
PL	$r_{DRM}^{PL} = k \cdot p_{CH_4}{}^{a} \cdot p_{CO_2}{}^{b}$	$r_{SRM}^{PL} = k \cdot p_{CH_4}{}^{a} \cdot p_{H_2O}{}^{b}$	$k = \frac{F_{CH_4}^{inlet}}{W_{cat}} \int_0^{X_{CH_4}^{outlet}} \frac{1}{r_{DRM/SRM}^{PL}} dX_{CH_4}$
LH	$r_{DRM}^{LH} = \frac{k p_{CH_4}{}^{a} p_{CO_2}{}^{b}}{\left(1 + K_{CH_4} p_{CH_4} + K_{CO_2} p_{CO_2}\right)^2} \times df$	$r_{SRM}^{LH} = \frac{k p_{CH_4}{}^{a} p_{H_2O}{}^{b}}{\left(1 + K_{CH_4} p_{CH_4} + K_{H_2O} p_{H_2O}\right)^2} \times df$	$k = \frac{F_{CH_4}^{inlet}}{W_{cat}} \int_0^{X_{CH_4}^{outlet}} \frac{1}{r_{DRM/SRM}^{LH}} dX_{CH_4}$

adsorption coefficient K_{CO_2} or steam adsorption coefficient K_{H_2O}. Table 5 outlines the functions and terminology utilized in this study.

3.1. Parameter estimation

The current study investigates the effects of temperature and current density on adsorption coefficients in DRM/SRM-SOFC using the Van't Hoff equation and Intrinsic kinetic models. Intrinsic kinetics, which focuses on reaction rates at the molecular level without transport phenomena interference, was explored for both processes. Understanding intrinsic kinetics is crucial for the accurate analysis of catalytic activity and reaction mechanisms. Kinetic measurements were conducted on a catalyst mass of 14.3 mg to minimise transport effects, in line with ICTAC kinetics committee recommendation of less than 1 g [39,44]. Using small catalyst masses in conjunction with a well-mixed reactor reduces heat and mass transfer effects, ensures uniform conditions, and maintains measurable reaction rates in this study. MATLAB was employed to iteratively estimate the pre-exponential factor (k_0) and activation energy (E_a), with reaction orders. E_a was calculated using a linear plot derived from the Arrhenius equation. The applicability of Langmuirian kinetics was assessed with thermodynamic parameters, requiring exothermic adsorption and entropy reduction. More details about the proposed models are available in the supplementary material.

Table 5

Terms and functions in DRM and SRM kinetic studies [7,26,32].

Term	Function		Definition
	DRM	SRM	
$\mathbf{K_{DRM/SRM}^{eq}}$	$6.78 \cdot 10^{14} \cdot \exp(\frac{-259660}{RT})$	$\exp(\frac{-26830}{T} + 30.114)$	The equilibrium constant of DRM/SRM
$\mathbf{K_{RWGS/WGS}^{eq}}$	$56.971 \cdot \exp(\frac{-35580}{RT})$	$\exp(\frac{4577.8}{T} - 4.33)$	RWGS/WGS equilibrium constant
df	$1 - \frac{p_{CO}{}^{2} p_{H_2}{}^{2}}{K_{DRM}^{eq} p_{CH_4} p_{CO_2}}$	$1 - \frac{p_{CO} p_{H_2}{}^{3}}{K_{SRM}^{eq} p_{CH_4} p_{H_2O}}$	Driving force
k	$k_0 \exp(\frac{-E_a^{DRM}}{RT})$	$k_0 \exp(\frac{-E_a^{SRM}}{RT})$	DRM/SRM Arrhenius expression for rate constant
$\mathbf{A_{CH_4}}$	6.65e-4		The pre-exponential adsorption constant of methane on the catalyst
$\mathbf{\Delta H_{CH_4}^0}$	−38.28		Adsorption enthalpy Changes (kJ/mol)
R	8.314		Universal gas constant (J/ (mol K))
$\mathbf{W_{cat}}$	14.3		Catalyst weight (mg)
K_j	$\exp(-\frac{\Delta G_j}{RT}) = A_j \cdot \exp(-\frac{\Delta H_j}{RT})$		adsorption coefficient based on Van't Hoff equation (bar^{-1})
$\mathbf{\Delta G_j^0}$	$\Delta G_j^0 = \Delta H_j^0 - T\Delta S_j^0$		Change of Gibbs free energy (kJ/ mol)
$\mathbf{\Delta S_{ad}^0}$	$\log(A_j) \times R$		Entropy of adsorption changes(J/mol.K)

4. Results and discussion

This research compares the electrocatalytic performance of an electrolyte-supported button cell SOFC utilizing NiO-GDC-YSZ as the anode material in DRM/SRM-SOFC. In the initial part of the study, we investigated the impact of key operational variables, gas composition, temperature, current density, and feed ratio on CH_4 conversion and reaction rates. Subsequent sections delve into the effects of current draw from fuel cells on adsorption parameters within the LH and PL models.

4.1. Impact of process parameters on CH_4 conversion rate

Fig. 2 illustrates the effects of current draw from the cell, fuel composition and cell temperature on CH_4 conversion rate. The graphs derived from the methane conversion equation outlined in Eq. (1) and data are also represented in Table 3.

The feed ratio for DRM-SOFC is expressed as $R_{DRM} = CH_4/CO_2$ and $R_{SRM} = CH_4/H_2O$ for the SRM-SOFC. Increased methane partial pressure in DRM (Fig. 2(a) to (c)) reduces methane conversion due to the mass action law. Higher R_{DRM} leads to undesired side reactions and catalyst saturation, decreasing efficiency. Conversely, lowering CH_4 in the fuel mixture enhances DRM conversion by better distributing reactants on the catalyst surface. Studies confirm that improving methane conversion involves reducing CH_4 or increasing CO_2 in the inlet gas [27,45–47]. The increase in methane conversion with increasing H_2O partial pressure in SRM is represented in Fig. 2(d) to (f). Lower R_{SRM} ratios provide more H_2O, facilitate effective CH_4 breakdown, and increase H_2 yield, as observed by Wojcik et al. [43]. High R_{SRM} ratios may lead to carbon formation due to insufficient water, while lower ratios minimize it, consistent with previous findings [8,10,22,32,35]. Optimal R_{SRM} ratios are critical, as excessively low ratios can introduce excess water, potentially cooling the reaction and impacting overall efficiency [48]. As shown in Table 3, methane conversion generally increases with current density, transitioning from open circuit to 1000 A/m^2 in all cases. The only exception is the case (vi) in SRM at 1073 K, where the methane conversion values at open circuit and 1000 A/m^2 are identical (0.286 or 28.6 %). It is worth noting that, in Fig. 2(e), a minor deviation is observed at an R_{SRM} value of 1.25, where the methane conversion at open circuit appears slightly higher than at 500 A/m^2. This deviation results from the curve-fitting method, as the data was interpolated using a spline function in MATLAB™.

Fig. 3(a) illustrates the impact of increasing R_{DRM} and R_{SRM} on methane conversion, as derived from the data presented in Table 3. SRM demonstrates higher methane conversion than DRM when equal CH_4 content is fed, highlighting H_2O's stronger influence as an oxidant over CO_2. This is due to SRM's lower enthalpy, leading to higher conversion under similar conditions. Exothermic side reactions like the WGS further enhance CH_4 consumption in SRM. Similar findings were reported by Yang et al.[10], who compared experimental data with ASPEN Plus™ software results, confirming this trend.

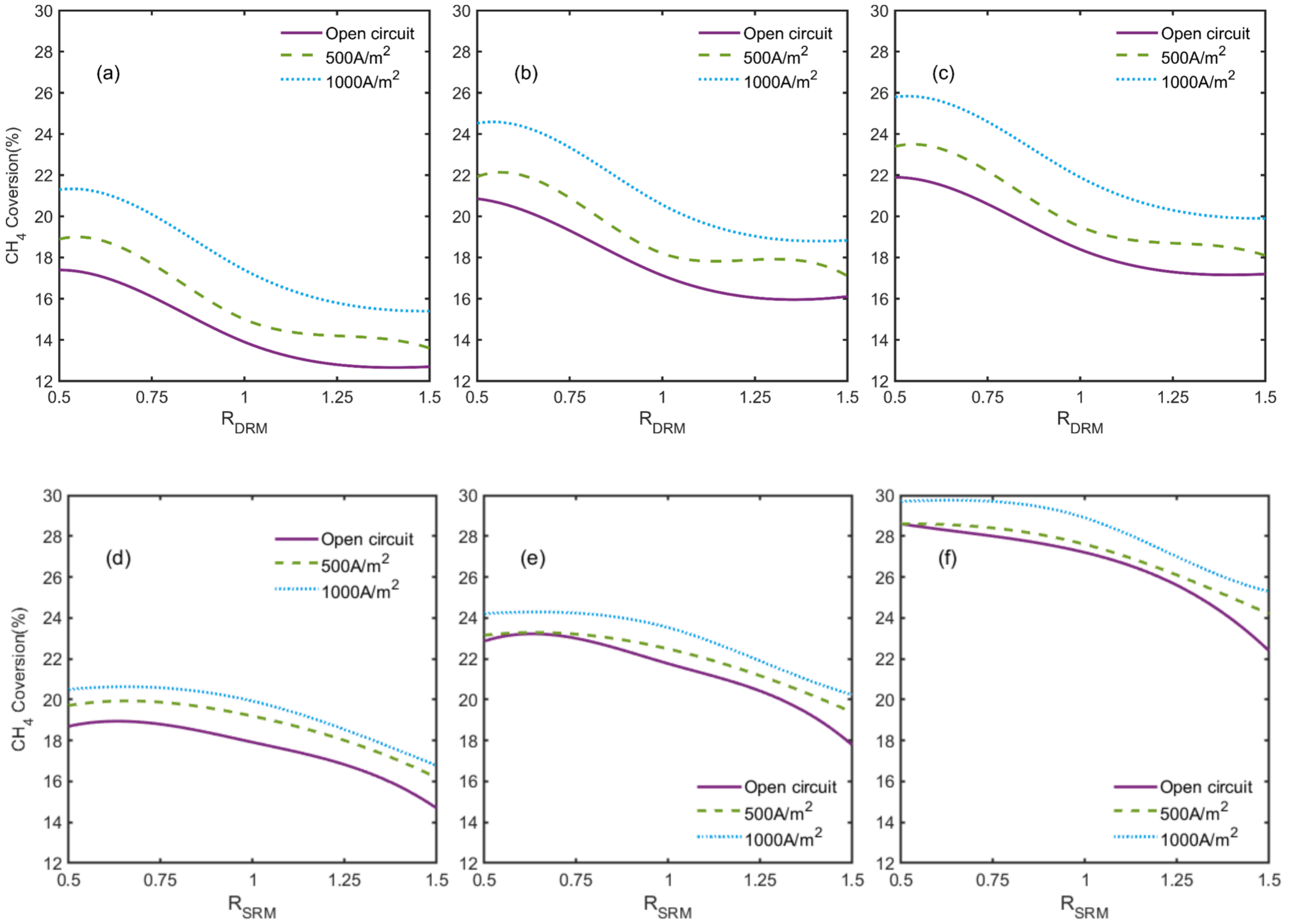

Fig. 2. Methane conversion behavior as a function of feed ratio at three temperatures for DRM [(a) 973 K, (b) 1023 K, (c) 1073 K] and SRM [(d) 973 K, (e) 1023 K, (f) 1073 K]. The solid purple line represents the open circuit voltage (OCV), while the dashed green line corresponds to a current density of 500 A/m^2. The dotted blue lines indicate the current density at 1000 A/m^2. (For interpretation of the references to colour in this figure legend, the reader is referred to the web version of this article.)

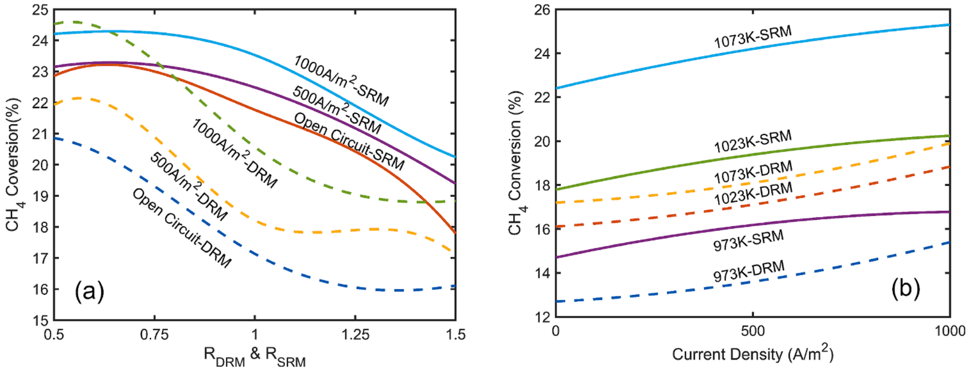

Fig. 3. (a) influence of feed ratio (R$_{DRM}$ & R$_{SRM}$) on methane conversion at a current density ranging from open-circuit, 500 A/m^2 and 1000 A/m^2; (b) Methane conversion behavior dependent on cell temperature for specific fuel composition at R$_{DRM}$, R$_{SRM}$ = 1.5, when current density changing from open circuit to 1000 A/m^2; The dashed lines indicates the DRM, whereas the solid lines represent SRM process.

Fig. 3(a) also compares the impact of current density on methane conversion, revealing an increase in methane conversion as electric current is applied. While SRM demonstrates a higher methane conversion rate than DRM, both processes exhibit a positive correlation between increasing current density and enhanced methane reforming rate. On the other hand, extracting a current from DRM has a more significant overall impact on methane conversion than SRM at the same feed ratio. Our findings align with Fan et al.[35] in SRM-SOFC, Lyu et al.[20] and Saadabadi et al.[27] for DRM-SOFC, indicating that an increased current density may correspond to a higher current density is linked to an enhanced transfer of electrons from the anode to the cathode. Another hypothesis links current density to oxygen flow rate, affecting anode fuel gas equilibrium and catalytic activity [35]. This scenario involves CH_4 oxidation into CO_2 and H_2O with oxygen ions, intensifying as current density rises. Studies like Zhou et al. [32] indicate that flowing oxygen ions at the triple-phase boundary (TPB) in Ni-GDC anodes boosts reaction rates in SRM-SOFC. Additionally, higher current density influences hydrogen consumption, shifting reforming reactions toward higher H_2 production and increased CH_4 consumption [5]. Temperature changes across the catalyst surface due to increased current density enhance endothermic catalytic interactions, increasing CH_4 conversion [40]. However, direct comparisons with other studies are challenging due to limited data on methane conversion rates and current density dependencies in DRM/SRM-SOFC under identical conditions. Future research is necessary to validate these findings comprehensively.

Since methane reforming is highly endothermic, temperature variations significantly influence both processes [10]. The temperature dependence of CH_4 conversion at specific R_{DRM} and R_{SRM} equal to 1.5 is illustrated in Fig. 3(b). For the DRM at a temperature of 973 K, methane conversion is relatively low and substantially increased as temperature rose. However, it remains lower than the SRM in the same temperature region. Our findings align with thermodynamic calculations [10,13,45,49] and other experimental works[27,43], indicating that increased temperature enhances the methane conversion rate.

SRM shows slightly higher methane conversion than DRM at similar temperatures due to better thermodynamics for removing carbon deposits. Thermodynamic calculations by Factsage™ software indicate that SRM produces 37 % less carbon deposition than DRM between 973 K and 1073 K, as depicted in Table 2 and Fig. 4(a). Increasing the H or O to C ratio makes carbon formation harder, leading to industrial SRM processes using high steam levels ($R_{SRM} \leq$ of 0.75, in this study), requiring substantial energy [9]. Lower carbon deposits in SRM promote more efficient methane conversion than DRM in this temperature range [50]. Additionally, the endothermic nature and temperature dependency of these processes enhances reactant conversion to products as the equilibrium constant depends on temperature [49].

4.2. Impact of operating conditions on hydrogen production

H_2 yield via SRM and DRM can be assessed from different perspectives, considering thermodynamic efficiency, and overall process performance. H_2 yield for each feed ratio in DRM and SRM from 973 k to 1073 based on thermodynamic calculations presented in Fig. 4(b). SRM exhibits higher H_2 efficiency than DRM at equivalent feed ratios. Additionally, it indicates that increasing CH_4 partial pressure has a more pronounced impact on DRM than on SRM. Specifically, the two processes have a substantial 57.6 % difference in the generated H_2 mol fraction. This observation implies that, under the specified circumstances, SRM may be more effective in H_2 yield. A potential reason for increased hydrogen production in SRM is that the byproduct CO reacts with H_2O in the forward WGS reaction, generating additional H_2. At the same time, changes in CH_4 partial pressure significantly influence the H_2 generation in DRM, with even slight changes leading to substantial variations in H_2 yield. These results align with those reported by Yang et al.[10]. While SRM is a well-established technology, exhibiting comparatively lower sensitivity to fluctuations in feed ratios, DRM shows promise for its benefits in carbon utilization and reduced greenhouse gas emissions, making it a more sustainable option for H_2 production and utilization in fuel cells.

4.3. Effects of operation parameters on reaction rate

The “reaction rate” refers to the change in concentrations of CH_4, H_2O, and CO_2 over time per unit of catalyst weight, also known as the “consumption rate of CH_4” in both processes [51], as described by the rate expressions. In this study, the reaction rate is determined using rate constants from the Arrhenius equation and reactant concentration data, as outlined in Table 4. Further details on the calculation procedure for the reaction rate can be found in the supplementary material. Catalytic activity is influenced by factors like cell temperature, current density, reactant feed ratios, catalyst type, and surface area [32,52]. Torimoto et al. found that SRM has a faster reaction rate than DRM due to more favorable thermodynamics and less carbon deposition on the catalyst surface, which can cause deactivation in DRM [46]. Various studies [23,32,35,53] have examined Ni-based catalysts for SRM-SOFCs under different conditions, showing varied SRM reaction rates due to different anode structures and process conditions. However, limited research compares SRM and DRM with the same fuel cell and oxidant quantities, making direct comparisons difficult due to variations in materials and conditions. Table 6 illustrates how operating conditions influence the reaction rate.

SRM reaction rates increase with cell temperature at various current densities, consistent with previous studies [22,23,52]. DRM shows a similar trend but with a lower magnitude. According to the collision model of chemical kinetics, reaction rates increase with temperature due to higher energy, more collisions and faster diffusion [54–56]. Higher temperatures also increase electronic and ionic conductivity in SOFCs, improving overall reaction kinetics [32]. The Arrhenius equation indicates that the rate constant rises exponentially with temperature, lowering the activation energy for methane reforming [57,58]. Moreover, elevated temperatures improve reactant access to catalyst active sites, increasing interactions and reaction rates. Additionally, higher temperatures reduce carbon deposition on the anode, potentially increasing reaction rates since fewer carbon molecules occupy catalyst active sites[14].

Both DRM and SRM reaction rates increase when subjected to an applied current, as illustrated in Fig. 5(a). An example at 1023 K shows the change from a feed ratio of 0.75 to 1.25. Fan et al. [35] attribute this

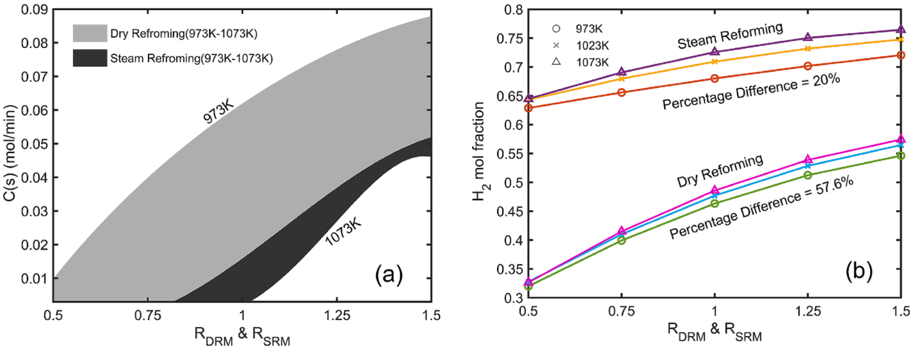

Fig. 4. (a) Carbon deposition possibility for each feed ratio in DRM and SRM from 973 k to 1073; The hatch black area corresponds to SRM and the hatch gray area is related to the DRM process. (b) Hydrogen production for each feed ratio in DRM and SRM from 973 k to 1073 based on FactSage™ Education 8.3 software calculations.

Table 6
Reaction rate analysis across operational conditions and current densities for DRM/SRM-SOFC.

		$r_{CH_4} \times 10^{-3}$ mol/s.g									
		DRM					SRM				
Temperature [K]	Current Density [A/m2]	i	ii	iii	iv	v	vi	vii	viii	ix	x
973	0	1.30	1.21	1.39	1.60	1.59	1.40	1.41	1.79	2.10	1.84
	500	1.42	1.33	1.50	1.77	1.70	1.48	1.49	1.92	2.25	2.02
	1000	1.60	1.51	1.74	1.97	1.92	1.54	1.54	1.99	2.32	2.10
1023	0	1.56	1.45	1.71	2.00	2.01	1.71	1.72	2.17	2.55	2.22
	500	1.64	1.57	1.82	2.23	2.14	1.73	1.74	2.25	2.64	2.42
	1000	1.84	1.75	2.05	2.38	2.35	1.81	1.82	2.35	2.73	2.53
1073	0	1.64	1.54	1.84	2.16	2.15	2.14	2.10	2.72	3.20	2.80
	500	1.75	1.66	1.95	2.34	2.26	2.14	2.13	2.76	3.26	3.02
	1000	1.93	1.84	2.19	2.53	2.49	2.23	2.23	2.89	3.37	3.16

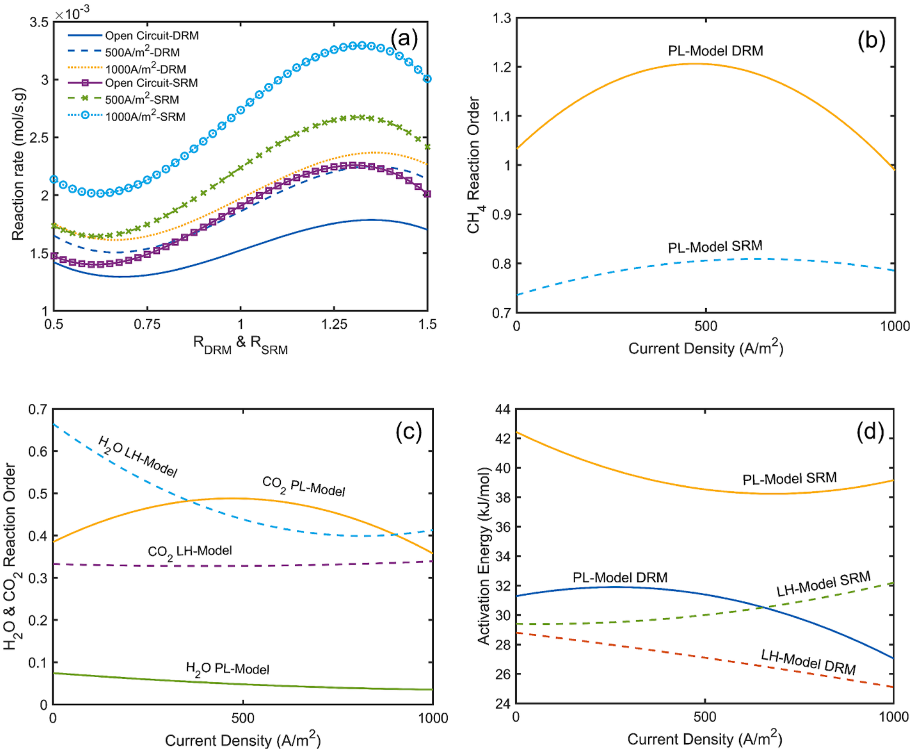

Fig. 5. (a) Reaction rates for DRM and SRM at 1023 K, illustrating variations across different current densities and R ratios. (b) Impact of current density drawn from the cell on reaction orders for methane, with the solid line representing DRM and the dashed line indicating SRM. (c) dependency of water and carbon dioxide reaction orders to current density changes; the purple dashed line related to the CO_2 reaction order for the LH model, the solid yellow line to the CO_2 reaction order based on the PL model, the blue dashed line to the H_2O reaction order according to the LH, and the solid green line to the H_2O reaction order from the PL model. (d) Relationship between current density and activation energy; the yellow solid line depicts E_a calculated using the PL model for the SRM process, the green dashed line for the LH model of the SRM process, the blue solid line for the PL model of the DRM process, and the red dashed line for the LH model of the DRM process. (For interpretation of the references to colour in this figure legend, the reader is referred to the web version of this article.)

to H_2 ion consumption, shifting the SRM reaction equilibrium toward higher conversion and increasing oxygen ion flux at the TPB, which boosts reaction rates. This flux enhancement also shifts the DRM equilibrium toward higher conversion. Higher current density creates a temperature gradient across the TPB [59], facilitating charge carrier transport across the electrolyte support layer and further influencing reaction rates. A more significant temperature gradient reduces carbon deposition and decreases the likelihood of active site occupation on the anode, ultimately enhancing reaction rates. Fig. 5(a) also shows the impact of R_{DRM} and R_{SRM} on reaction rates, revealing that higher oxidant partial pressure negatively affects reaction rates. As observed in prior studies, increasing CH_4 partial pressure boosts SRM and DRM rates [32,35,52]. Wang et al. [60] found that DRM rates rise with more CH_4 but drop with higher CO_2, significantly influencing reaction rates. Low R_{DRM} or R_{SRM} values show a flatter trend that increases with rising values. This can be due to oxidant partial pressure diluting CH_4 partial pressure under constant total reaction pressure [37], and competition for adsorption between oxidant and CH_4 on anode active sites [35]. Proper feeding ratios optimize fuel utilization, carbon deposition, and SOFC performance. Typical R_{SRM} for SRM is 0.3–0.4 [7,43,48], while DRM's higher carbon-to-hydrogen ratio requires an R_{DRM} of 1–1.5 for efficient syngas production [9,37]. Higher reaction rates don't always mean optimal conditions, as carbon deposition, catalyst degradation, and syngas production must also be considered.

4.4. *Impact of electrochemical reaction on kinetic parameters*

In this study, we employed optimization techniques that utilized a data fitting methodology, using the "interior-point" algorithm by the "fmincon" function in MATLAB™. This enabled us to identify the optimal values for the kinetics of absorption and the constants related to reaction rates. Our approach accounted for a range of experimental data and constraints, as outlined in section 3.3. The resulting kinetic parameters for DRM and SRM were derived, including aspects such as adsorption enthalpy, entropy, reaction orders, pre-exponential factors and activation energy associated with these models, as presented in Table 7.

4.5. *Methane reaction order*

The higher and positive reaction orders for methane obtained from the PL model at different current densities suggest that DRM and SRM are more sensitive to changes in CH_4 partial pressure than the oxidant's partial pressure. As illustrated in Fig. 5(b), the calculated CH_4 reaction orders exhibit an initial increase with a slight current draw, followed by a decrease with higher current densities. A peak is observed at a current density of 500 A/m^2, which aligns with the studies conducted by Fan et al.[35], Zhou et al.[32] for the SRM-SOFC and Moarrefi et al.[40] for DRM-SOFC. The graph also illustrates that the dependency of the reaction rate on methane concentration is notably higher in the DRM compared to the SRM. Previous studies also indicate that, under low-pressure conditions, the reaction rate shows almost a first-order correlation with CH_4 partial pressure and is nearly unaffected by oxidants' partial pressure[60].

4.6. *Oxidants' reaction orders*

The reaction order concerning H_2O partial pressure can vary, being negative, zero, or positive, primarily depending on the R_{SRM} ratio, as indicated by numerous studies [61]. The H_2O reaction order varied significantly in the LH model compared to the PL model, being higher under open-circuit than closed-circuit conditions, as shown in Fig. 5(c). As a partial conclusion, with increasing current density under low-pressure conditions, the CH_4 consumption rate has a first-order correlation with its partial pressure. It is almost more independent of the H_2O partial pressure in higher current densities. However, our study reveals that, besides temperature and feed ratio variables, current density also impacts H_2O reaction order. At the same time, its relatively low quantity aligns with findings in the literature [32,35]. The CO_2 reaction order in the LH model is lower than the order for H_2O and CH_4. This lower CO_2 reaction order is typical for the DRM[37]. The reaction order of CO_2 in the PL model peaks at 500 A/m^2, while the H_2O reaction order consistently decreases with increasing current density. In the LH model, the CO_2 reaction order is relatively stable with a slight increase at higher current density, while the H_2O reaction order significantly decreases as current density increases. When examining the reaction orders for oxidants, H_2O concentration has a greater impact on the CH_4 consumption rate than CO_2 in the LH model. The CO_2 reaction order calculated demonstrates similar values under open and closed-circuit conditions in both proposed models, indicating that this parameter is relatively independent of the current densities investigated in this study.

Table 7
Calculated PL and LH kinetic model parameters at various current densities.

Kinetic Parameters	Current Density [A/m^2]	PL-DRM	PL-SRM	LH-DRM	LH-SRM
a	0	1.03	0.74	1	1
	500	1.21	0.81	1	1
	1000	0.99	0.79	1	1
b	0	0.38	0.07	0.33	0.66
	500	0.49	0.05	0.33	0.44
	1000	0.36	0.04	0.34	0.41
Ea (kJ/mol)	0	31.3	42.4	28.8	29.4
	500	31.4	38.5	27.1	30
	1000	27.0	39.2	25.1	32
$\mathbf{K_j}$(bar^{-1})	0	–	–	8.03E-08	0.61
	500	–	–	4.79E-09	0.40
	1000	–	–	1.39E-08	0.36
$\Delta\mathbf{H_j^0}$(kJ/mol)	0	–	–	−7.3	−40.6
	500	–	–	−7.2	−36.7
	1000	–	–	−7.4	−35.8
$\Delta\mathbf{S_j^0}$(J/mol. K)	0	–	–	−142.6	−42
	500	–	–	−166.0	−42
	1000	–	–	−157.4	−42

4.7. *Activation energy*

It is widely accepted that the reduced activation energy of a reaction compared to the initial state in a catalyst represents improving the catalytic activity of a material[62]. Fig. 5(d) shows that activation energy depends on current density in DRM/SRM-SOFC models. The DRM activation energy in the PL model shows stability up to 500 A/m^2, followed by a notable decrease at 1000 A/m^2, suggesting a reduction in energy required for DRM at higher current densities. The SRM activation energy in the PL model decreases initially but increases slightly at higher current densities, indicating a complex dependence on current density. In the LH model, the DRM activation energy consistently decreases with increasing current density, indicating a reduction in activation energy requirements. The SRM activation energy in the LH model shows an increasing trend with current density, suggesting higher energy requirements at higher current densities. The PL model estimates higher activation energy than the LH model, aligning with Fan et al. [23,35] and Zhou et al.[32] findings on the SRM-SOFC. Fan et al.[35] attribute this to O^{2-} ions from adsorbed H_2O dissociation, which alleviate H_2O partial pressure effects in SRM. Increased current density improves oxygen ion movement in the electrolyte, aiding carbon oxidation and surface cleaning, as emphasized by Hussien et al. [14]. Zhou et al.[32] suggested that steam indirectly influences the reaction rate by affecting the activation of methane, particularly through its concentration-dependent impact on adsorbed OH groups, which could be related to the Grotthuss mechanism in the SRM. The Grotthuss mechanism refers to a proton transfer mechanism that involves the migration of protons along a chain of hydrogen-bonded water molecules[63]. In SRM, the Grotthuss mechanism can be associated with protons' role in facilitating methane dissociation into reactive species. Also, they concluded that the O^{2-} flux is influencing reforming rates, with mechanisms like the Classic Motts-Cabrera field-assisted growth, which plays a role in facilitating ion movement through the oxide film formed on the catalyst/anode surface[64]. The proposed mechanism provides a theoretical framework for understanding the oxidation of metals used as a catalyst for SOFCs. According to this model, there is an equilibrium in the distribution of electrons from the metal at the catalyst layer to the surface covered with oxygen adsorbates. As the oxide layer grows, the movement of ions across electrolytes is facilitated by an electric field generated by the Cabrera-Mott potential[65]. This electric field arises from the negative charge on the adsorbed oxygen anions and the corresponding positive charge on the metal side, creating a scenario like a parallel plate capacitor[32]. In conclusion, the dissociative adsorption of H_2O and the quantity of generated OH groups are crucial in increased proton conductivity, enhancing catalyst activity and reducing activation energy in SRM under an electric field.

Due to the chemical stability of CO_2 molecules and the highly endothermic nature of the reaction, DRM requires more energy input than SRM to overcome the activation energy[15]. This finding contrasts with the results of this study, where the DRM shows a lower activation energy for converting CH_4 and CO_2 molecules into products. This outcome directs our attention to the use of R^2 (R-squared) and RMSE (Root Mean Square Error) statistical methods to evaluate the performance and accuracy of regression models for the estimation of activation energies. Table 8 provides the Arrhenius equation and associated R^2 and RMSE values for the rate constants.

Table 8
Arrhenius equation for rate constant for DRM/SRM.

Process	Current Density [A/m^2]	PL	R^2	RMSE	LH	R^2	RMSE
SRM	0	$k = 7.68e^{-1}\exp(\frac{5105}{T})$	0.973	0.0402	$k = 7.22e^{-1}\exp(\frac{3536}{T})$	0.995	0.0245
	500	$k = 5.35e^{-1}\exp(\frac{4634}{T})$	0.967	0.0455	$k = 5.38e^{-1}\exp(\frac{3608}{T})$	0.988	0.0347
	1000	$k = 5.81e^{-1}\exp(\frac{4710}{T})$	0.975	0.0419	$k = 6.97e^{-1}\exp(\frac{3873}{T})$	0.99	0.0314
DRM	0	$k = 2.79e^{-1}\exp(\frac{3672}{T})$	0.932	0.0633	$k = 1.99e^{-1}\exp(\frac{3464}{T})$	0.938	0.0656
	500	$k = 4.17e^{-1}\exp(\frac{3776}{T})$	0.929	0.0613	$k = 1.79e^{-1}\exp(\frac{3260}{T})$	0.937	0.0665
	1000	$k = 1.99e^{-1}\exp(\frac{3252}{T})$	0.940	0.0515	$k = 1.64e^{-1}\exp(\frac{3019}{T})$	0.937	0.053

Higher R^2 values indicate better model fit, and lower RMSE values indicate better accuracy. SRM shows smaller RMSE and higher R^2 than DRM in simulated Arrhenius plots of activation energies, indicating more accurate E_a estimation for SRM. Further validation is needed for DRM-SOFC because it is the first study of its kind. An R^2 value of approximately 0.93 for DRM indicates reasonable accuracy, demonstrating promising results. Notably, R^2 values exceeding 0.9 reflect strong correlations. The minor difference between the two R^2 values has minimal impact on the DRM model's reliability, as it still accounts for over 93 % of the variance. SRM and DRM exhibit reduced activation energies during electrochemical reactions in SOFCs, suggesting similar phenomena. More research is needed to fully understand these effects on E_a variation. Several reasons may also contribute to this variation:

- Implementing a current or voltage across a fuel cell could facilitate non-spontaneous chemical reactions. This external energy reduces the E_a by supplying the required energy for the oxidation of species, ultimately enabling the reaction to proceed[66].
- Higher temperatures imposed by electrochemical reactions on a SOFC anode may increase the kinetic energy of reactant molecules across TPB, aiding reactants in overcoming the E_a for transferring to products more efficiently[67].

Previous studies suggest that E_a tends to be higher in PL models compared to LH models, mainly due to PL models' omission of surface chemistry factors like carbon deposition or the Grotthuss mechanism [36,42]. Additionally, increasing current in electrochemical devices promote oxidative reactions on the catalyst, thereby lowering apparent E_a and favoring product formation [64,65]. Our research affirms LH models as superior for predicting kinetic parameters due to their higher R^2 and lower RMSE values, which align better with experimental data and consider surface heterogeneity, making them reliable for reactions involving adsorption [17]. The applicability of the Arrhenius equation in this study was evaluated, even though no directly comparable studies exist for the selected materials under the same conditions. For the SRM process, the activation energy and pre-exponential factor match with the trends and values reported by Fan et al.[35], showing no significant deviations. For the DRM process, similar studies are unavailable, so statistical methods were used to validate the Arrhenius equation parameters. High R^2 and low RMSE values indicate a strong fit between the experimental data and the predicted rate constants. The Arrhenius parameters remained consistent and meaningful across changes in reactant composition, temperature and current density. However, future studies under similar conditions are needed to fully validate the results, especially for the DRM process.

4.8. Adsorption parameters

This study also aimed to compare the effects of electrochemical interactions on the adsorption kinetics. The adsorption equilibrium constant (K_j) is a thermodynamic parameter that quantifies the ratio of the concentration of adsorbed molecules on a surface to the concentration of the same molecules in the reaction at equilibrium[57,68]. The primary stages in internal DRM/SRM-SOFC consist of CH_4 and oxidant adsorption at the catalyst's surface, leading to carbon monoxide and hydrogen production and the final desorption of the syngas products[24,25]. A higher value of K_j indicates a strong affinity of the adsorbate on the surface at that specified current density level.

The specific numerical values derived for H_2O and CO_2 adsorption parameters have been presented in Table 7. Fig. 6(a) illustrates the relationship between the oxidant's adsorption equilibrium coefficient and current density. In open-circuit conditions, where there is no electron transfer from the anodic reactions, the adsorption coefficients for H_2O and CO_2 are greater than those observed under closed-circuit conditions. This phenomenon arises from the considerable charge accumulation on the catalyst surface, necessitating many cations and anions to balance the charge [32]. H_2O exhibits a higher affinity to the anode's surface than CO_2, as evidenced by its notably greater adsorption coefficient at the same current density level. The decrease in adsorption coefficient at a current density of 750 A/m2 suggests a reduction in electron or charge accumulation on the electrode's surface when current is drawn, necessitating fewer counter ions. At a higher current density of 1000 A/m2, a slight increase in the adsorption equilibrium coefficient for both CO_2 and H_2O are observed, possibly due to the higher current density exceeding the limit where the assumption of dissociative adsorption of oxidant molecules is no longer valid. Similar effects reported in the SRM may also apply to the DRM [32,35].

Furthermore, examining the alterations in enthalpy and entropy associated with oxidants' adsorption over SOFCs provides crucial insights into the thermodynamic perspective of the adsorption mechanism. The enthalpy change (ΔH_j^0) represents the heat absorbed or released during adsorption. In contrast, a positive entropy change (ΔS_j^0) indicates an increase in disorder, while a negative entropy change indicates a decrease in disorder. Fig. 6(b) illustrates the influences of current density on adsorption enthalpy and entropy of CO_2 and H_2O molecules. The negative value of $\Delta H_{H_2O}^0$ and $\Delta H_{CO_2}^0$ indicate an exothermic behaviour of the adsorption in SOFC, indicating the heat release when both oxidant molecules are attached onto the anode. This implies that the H_2O and CO_2 adsorption is thermodynamically favorable. Comparing the enthalpy changes for both species reveals that H_2O adsorption is more exothermic than the adsorption of CO_2 species. Moreover, the data indicates that rising current density exerts a more pronounced effect on the enthalpy variations of H_2O than on those of CO_2. Freund et al.[69] stated that the chemical stability of CO_2 molecules is higher than that of H_2O, which could explain the slight changes of adsorption enthalpy of CO_2 from the current density drawn by the fuel cell. The substantial difference in the negative values of $\Delta S_{CO_2}^0$ and $\Delta S_{H_2O}^0$, with the former being almost four times as low as the latter, indicates that the adsorption of CO_2 via DRM tends toward a more ordered (less disordered) state than the adsorption of H_2O in SRM. Furthermore, it is observed that the influence of current density on the

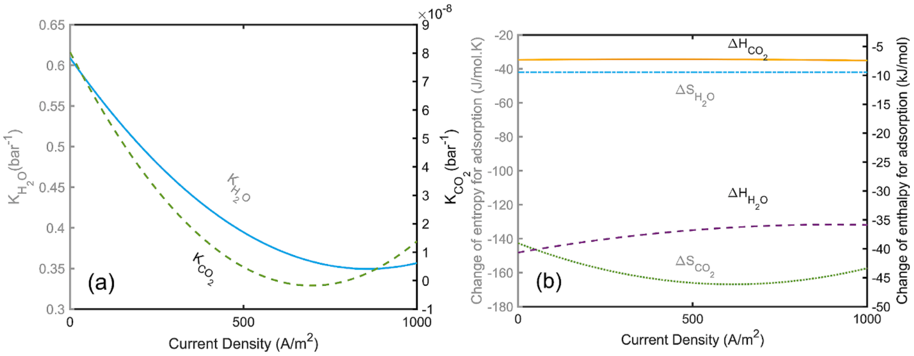

Fig. 6. (a) Examination of the relationship between current density and the equilibrium coefficients for CO_2 and H_2O adsorption; the dashed green line indicates the CO_2 equilibrium coefficient, while the solid blue line represents the H_2O equilibrium coefficient. (b) Assessment of the impact of current density on adsorption enthalpy and entropy; the solid yellow line illustrates the enthalpy associated with CO_2 adsorption, the dash-dotted blue line shows the entropy related to H_2O adsorption, the dashed purple line depicts the enthalpy for H_2O adsorption, and the dotted green line reflects the entropy for CO_2 adsorption. (For interpretation of the references to colour in this figure legend, the reader is referred to the web version of this article.)

entropy change of steam is nearly negligible. This implies that SRM operates independently of current density effects on its system entropy. In the case of DRM, draw a current, decrease the entropy value of CO_2 adsorption, and increase it with a higher current density applied, leading to a more ordered state than the open circuit set point. This suggests that the effect of current density on entropy change is more significant for CO_2 adsorption during DRM, indicating a stronger bonding of CO_2 species to active sites on the anode. The same trends for the effect of current density on oxidant adsorption parameters were reported by Fan et al.[35] in SRM-SOFC were also observed in our recent study[40] at a different temperature range in DRM-SOFC. This indicates that the results are reliable and comparable when considering both processes on the same fuel cell. Given the wider temperature range investigated in this study, a broader range of current densities is highly recommended to determine the exact reasons behind these observations.

5. Conclusions

This study investigates the impact of operating conditions on CO_2 and H_2O adsorption in button fuel cells with Ni-GDC and Ni-YSZ anodes, contributing to understanding reaction kinetics and electrochemical reactions in SOFC reforming. These insights are crucial for advancing cleaner energy production. SRM and DRM are two key methods for producing syngas from methane SRM is effective for hydrogen production at high temperatures, while DRM helps reduce CO_2 emissions by converting methane and CO_2 into hydrogen and carbon monoxide. Both processes benefit from electrochemical reactions in SOFCs to improve efficiency. Small catalyst masses were combined with a well-mixed reactor to ensure uniform conditions and reduce heat and mass transfer effects, allowing for reliable reporting of intrinsic kinetics parameters. Comparing the kinetics of SRM and DRM is essential for optimizing anode design under different conditions.

Key findings:

- **Hydrogen production and methane conversion:** SRM shows higher hydrogen production and methane conversion than DRM with the same CH_4 feed, and both processes see increased conversion with rising current density, with SRM consistently outperforming DRM. Higher R_{DRM} and R_{SRM} reduce overall methane conversion while decreasing CH_4 content in the feed improves it. The PL model suggests that methane conversion in DRM is more sensitive to CH_4 partial pressure changes than SRM.
- **Reaction rates:** Methane reforming reaction rates increase with CH_4 partial pressure in the feed due to reduced oxidant pressure and enhanced adsorption competition on the anode surface. Both processes have temperature and current-dependent reaction rates, but DRM has a lower CH_4 consumption rate than SRM.
- **Activation energy trends:** The LH model shows CO_2 in DRM has a greater impact on kinetic parameters than H_2O in SRM. SRM's activation energy decreases slightly with increasing current density before rising again. Meanwhile, DRM shows a continuous decline in activation energy with current drawn from the cell. SRM demonstrates higher accuracy in estimating activation energy, as indicated by lower RMSE and higher R^2 values than DRM. Although DRM's activation energy is lower than SRM's, this contrast with previous studies is due to the SRM model's better accuracy. Nonetheless, DRM still shows promising results with an R^2 value of ~ 0.95.
- **Thermodynamics of adsorption:** Negative ΔH_j^0 values indicate exothermic adsorption, with H2O being more exothermic than CO_2. Current density affects H_2O's enthalpy changes more than CO_2, which remains unaffected by the current draw from the cell. Differences in ΔS_j^0 suggest CO_2 adsorption is more ordered in DRM than H_2O in SRM. Current density has little effect on H_2O entropy, but increased current leads to a more ordered state for CO_2 molecules in DRM. Under open-circuit conditions, both H_2O and CO_2 exhibit higher adsorption coefficients than in closed-circuit, with H_2O having a significantly greater coefficient than CO_2 at the same current density.

These findings deepen our understanding of DRM and SRM inside SOFCs, providing crucial insights for optimizing electrocatalytic processes. It helps develop advanced anode materials, offering better catalytic activity and resist issues like carbon buildup and sulfur poisoning. These improvements are especially important for distributed energy systems using SOFCs that require flexible and reliable fuel options. As we delve into the complexities of electrochemical reactions in SOFCs, additional research is still needed to fully comprehend the potential of this promising technology.

5.1. Hints for future research

- Understanding intrinsic kinetics is crucial for accurately determining catalytic activity and reaction mechanisms, free from heat and mass transport limitations. Future studies could examine different flow rates to evaluate external diffusion limitations. If the reaction rate remains unchanged with increasing flow, external diffusion is minimal and intrinsic kinetic parameters are reliable. Alternatively, the Mears criterion or Carberry number could be used to assess external mass transfer limitations, where values below critical thresholds indicate negligible diffusion.

- Kinetics of syngas reforming in carbon dioxide and steam mixtures, representing actual syngas compositions in SOFCs. This will provide valuable insights into how temperature and current density influence reforming kinetics under practical conditions.
- Current reaction rate functions in simulation studies rely on temperature-dependent equations for DRM and SRM, which may lack accuracy as kinetic parameters vary with increasing current density. Developing universal rate equations that account for temperature and current density effects will improve the accuracy and reliability of SOFC simulation studies.

CRediT authorship contribution statement

Saeed Moarrefi: Writing – review & editing, Writing – original draft, Methodology, Investigation, Formal analysis, Data curation, Conceptualization. **Mohan Jacob:** Writing – review & editing, Funding acquisition. **Nilay Shah:** Writing – review & editing. **Stephen Skinner:** Writing – review & editing. **Weiwei Cai:** Writing – review & editing, Investigation. **Liyuan Fan:** Writing – review & editing, Supervision, Project administration, Investigation, Funding acquisition, Conceptualization.

Declaration of competing interest

The authors declare that they have no known competing financial interests or personal relationships that could have appeared to influence the work reported in this paper.

Acknowledgement

The authors thank James Cook University, Australia, for providing educational resources and the International Collaboration for Hydrogen Research Program, Australia, for supporting international research collaborations.

Appendix A. Supplementary data

Supplementary data to this article can be found online at https://doi.org/10.1016/j.fuel.2025.134413.

Data availability

Data will be made available on request.

References

[1] U.N.F.C.o.C. Change, The Paris Agreement UNFCCC, Paris, France, 2015, p. 27.

[2] U. Secretariat, Report of the Conference of the Parties on its twenty-first session, held in Paris from 30 November to 13 December 2015, 2016. https://unfccc.int/documents/9097. (Accessed 29 jan 2016).

[3] Meinshausen M, Lewis J, McGlade C, Gütschow J, Nicholls Z, Burdon R, et al. Realization of Paris Agreement pledges may limit warming just below 2 °C. Nature 2022;604(7905):304–9. https://doi.org/10.1038/s41586-022-04553-z.

[4] Atkinson A, Barnett S, Gorte RJ, Irvine JTS, McEvoy AJ, Mogensen M, et al. Advanced anodes for high-temperature fuel cells. Nat Mater 2004;3(1):17–27. https://doi.org/10.1038/nmat1040.

[5] Fan L, Li Ce, Aravind PV, Cai W, Han M, Brandon N. Methane reforming in solid oxide fuel cells: Challenges and strategies. Journal of power sources 538 2022. https://doi.org/10.1016/j.jpowsour.2022.231573.

[6] Faheem HH, Britt B, Rocha M, Zhou S-H, Li Ce, Cai W, Fan L. Sensitivity analysis and process optimization for biomass processing in an integrated gasifier-solid oxide fuel cell system. Fuel 356 2024:129529. https://doi.org/10.1016/j.fuel.2023.129529.

[7] Fan L, Li Ce, van Biert L, Zhou S-H, Tabish AN, Mokhov A, Aravind PV, Cai W. Advances on methane reforming in solid oxide fuel cells. Renewable and Sustainable Energy Reviews 166 2022:112646. https://doi.org/10.1016/j.rser.2022.112646.

[8] van Biert L, Visser K, Aravind PV. A comparison of steam reforming concepts in solid oxide fuel cell systems. Appl Energy 2020;264. https://doi.org/10.1016/j.apenergy.2020.114748.

[9] Torimoto M, Sekine Y. Effects of alloying for steam or dry reforming of methane: a review of recent studies. Cat Sci Technol 2022;12(11):3387–411. https://doi.org/10.1039/D2CY00066K.

[10] Yang P, Zhang Y, Yang C, Chen J, Liu Z, Deng C, et al. Thermodynamic performance comparison of a SOFC system integrated with steam reforming and dry reforming by utilizing different fuels. Energ Conver Manage 2024;300:117981. https://doi.org/10.1016/j.enconman.2023.117981.

[11] Liu H, Dong M, Xiong J, Yang J, Ning J, Liang Y, et al. CO2 laser promoted oxygen vacancy-active oxygen cycle in DRM on Ni/CeO2. Energ Conver Manage 2023;286:117081. https://doi.org/10.1016/j.enconman.2023.117081.

[12] P. Singh, B. Hu, Advanced Anode for Internal Reforming and Thermal Management in Solid Oxide Fuel Cells, United States, 2020, p. Medium: ED; Size: 17 p.

[13] Soleimani S, Lehner M. Tri-reforming of methane: thermodynamics, operating conditions, reactor technology and efficiency evaluation—a review. Energies 2022;15(19):7159.

[14] Hussien AGS, Polychronopoulou K. A review on the different aspects and challenges of the dry reforming of methane (DRM) reaction. Nanomaterials 2022;12(19):3400.

[15] Ighalo JO, Amama PB. Recent advances in the catalysis of steam reforming of methane (SRM). Int J Hydrogen Energy 2024;51:688–700. https://doi.org/10.1016/j.ijhydene.2023.10.177.

[16] Liu H, Dong M, Xiong J, Huang Z, Hou H, Liang Y, et al. Study on Ce-MOF-derived oxides as morphology-tunable catalyst supports for dry reforming of methane. Appl Surf Sci 2025;679:161167. https://doi.org/10.1016/j.apsusc.2024.161167.

[17] Faheem HH, Abbas SZ, Tabish AN, Fan L, Maqbool F. A review on mathematical modelling of direct internal reforming- solid oxide fuel cells. J Power Sources 2022;520:230857. https://doi.org/10.1016/j.jpowsour.2021.230857.

[18] Lyu Z, Li H, Han M. Electrochemical properties and thermal neutral state of solid oxide fuel cells with direct internal reforming of methane. Int J Hydrogen Energy 2019;44(23):12151–62. https://doi.org/10.1016/j.ijhydene.2019.03.048.

[19] Saadabadi SA, Thallam Thattai A, Fan L, Lindeboom REF, Spanjers H, Aravind PV. Solid oxide fuel cells fuelled with biogas: potential and constraints. Renew Energy 2019;134:194–214.

[20] Lyu Z, Shi W, Han M. Electrochemical characteristics and carbon tolerance of solid oxide fuel cells with direct internal dry reforming of methane. Appl Energy 2018;228:556–67. https://doi.org/10.1016/j.apenergy.2018.06.114.

[21] Najafi Maharluie H, Rahmani M. Mathematical modeling of solid oxide fuel cell performance with indirect internal reforming and thermal interaction analysis. Energy Conversion and Management 316 2024:118842. https://doi.org/10.1016/j.enconman.2024.118842.

[22] Hou K, Hughes R. The kinetics of methane steam reforming over a Ni/α-Al2O catalyst. Chem Eng J 2001;82(1):311–28. https://doi.org/10.1016/S1385-8947(00)00367-3.

[23] Fan L, van Biert L, Thallam Thattai A, Verkooijen AHM, Aravind PV. Study of methane steam reforming kinetics in operating solid oxide fuel cells: influence of current density. Int J Hydrogen Energy 2015;40(15):5150–9. https://doi.org/10.1016/j.ijhydene.2015.02.096.

[24] Abdullah B, Abd Ghani NA, Vo D-V-N. Recent advances in dry reforming of methane over Ni-based catalysts. J Clean Prod 2017;162:170–85. https://doi.org/10.1016/j.jclepro.2017.05.176.

[25] Mogensen D, Grunwaldt JD, Hendriksen PV, Dam-Johansen K, Nielsen JU. Internal steam reforming in solid oxide fuel cells: Status and opportunities of kinetic studies and their impact on modelling. J Power Sources 2011;196(1):25–38. https://doi.org/10.1016/j.jpowsour.2010.06.091.

[26] Thallam Thattai A, van Biert L, Aravind PV. On direct internal methane steam reforming kinetics in operating solid oxide fuel cells with nickel-ceria anodes. Journal of Power Sources 370 2017:71–86. https://doi.org/10.1016/j.jpowsour.2017.09.082.

[27] Saadabadi SA, Illathukandy B, Aravind PV. Direct internal methane reforming in biogas fuelled solid oxide fuel cell; the influence of operating parameters. Energy Sci Eng 2021;9(8):1232–48. https://doi.org/10.1002/ese3.887.

[28] Lee MS, Kim YJ, Hwang J, Choi I, Yu W, Lee YH, et al. Effect of Ni–GDC anode thickness by Co-sputtering on the high-performance thin film solid oxide fuel cells on a nanoporous substrate for low-temperature operation. J Power Sources 2023;555:232376. https://doi.org/10.1016/j.jpowsour.2022.232376.

[29] Khan MS, Miura Y, Fukuyama Y, Gao S, Zhu Z. Methane internal steam reforming in solid oxide fuel cells at intermediate temperatures. Int J Hydrogen Energy 2022;47(29):13969–79. https://doi.org/10.1016/j.ijhydene.2022.02.128.

[30] Sakama S, Chanthanumataporn M, Hanamura K. Carbon deposition influenced by gas concentration in a Ni/YSZ anode of an internal-reforming solid oxide fuel cell using a detector layer inside the anode. J Power Sources 2022;551:232153. https://doi.org/10.1016/j.jpowsour.2022.232153.

[31] Bian Z, Wang Z, Jiang B, Hongmanorom P, Zhong W, Kawi S. A review on perovskite catalysts for reforming of methane to hydrogen production. Renew Sustain Energy Rev 2020;134:110291. https://doi.org/10.1016/j.rser.2020.110291.

[32] Zhou S-H, Omanga E, Tabish AN, Cai W, Fan L. Effect of electrochemical reaction on steam adsorption during methane reforming on a Ni-GDC anode. Fuel 2023;332:125973. https://doi.org/10.1016/j.fuel.2022.125973.

[33] Hurtado P, Ordóñez S, Sastre H, Díez FV. Development of a kinetic model for the oxidation of methane over Pd/Al2O3 at dry and wet conditions. Appl Catal B 2004;51(4):229–38. https://doi.org/10.1016/j.apcatb.2004.03.006.

[34] Kumar KV, Porkodi K, Rocha F. Langmuir–Hinshelwood kinetics – A theoretical study. Catal Commun 2008;9(1):82–4. https://doi.org/10.1016/j.catcom.2007.05.019.

[35] Fan L, Mokhov A, Saadabadi SA, Brandon N, Aravind PV. Methane steam reforming reaction in solid oxide fuel cells: influence of electrochemical reaction and anode thickness. J Power Sources 2021;507:230276. https://doi.org/10.1016/j.jpowsour.2021.230276.

[36] Pino L, Italiano C, Laganà M, Vita A, Recupero V. Kinetic study of the methane dry (CO2) reforming reaction over the Ce0.70La0.20Ni0.10O2−δ catalyst. Cat Sci Technol 2020;10(8):2652–62. https://doi.org/10.1039/C9CY02192B.

[37] Özkara-Aydınoğlu Ş, Erhan Aksoylu A. A comparative study on the kinetics of carbon dioxide reforming of methane over Pt–Ni/Al2O3 catalyst: effect of Pt/Ni ratio. Chemical Engineering Journal 215-216 2013:542–9. https://doi.org/10.1016/j.cej.2012.11.034.

[38] Wójcik M, Szabłowski Ł, Dybiński O. Comparison of mathematical models of steam methane reforming process for the needs of fuel cells. Int J Hydrogen Energy 2023. https://doi.org/10.1016/j.ijhydene.2023.08.293.

[39] Vyazovkin S, Burnham AK, Criado JM, Pérez-Maqueda LA, Popescu C, Sbirrazzuoli N. ICTAC Kinetics Committee recommendations for performing kinetic computations on thermal analysis data. Thermochim Acta 2011;520(1):1–19. https://doi.org/10.1016/j.tca.2011.03.034.

[40] Moarrefi S, Jacob M, Li Ce, Cai W, Fan L. Internal dry reforming of methane in solid oxide fuel cells. Chemical Engineering Journal 489 2024:151281. https://doi.org/10.1016/j.cej.2024.151281.

[41] M. Seabaugh, NextCell Versus NextCell-HP: Comparing Performance Data, 2017. https://fuelcellmaterials.com/nextcell-versus-nextcell-hp-comparing-performance-data/. (Accessed October 11 2017).

[42] Vannice MA. Kinetic data analysis and evaluation of model parameters for uniform (ideal) surfaces. In: Vannice MA, editor. Kinetics of Catalytic Reactions. US, Boston, MA: Springer; 2005. p. 106–40. 10.1007/978-0-387-25972-7_6.

[43] Wójcik M, Szabłowski Ł, Dybiński O. Comparison of mathematical models of steam methane reforming process for the needs of fuel cells. Int J Hydrogen Energy 2024; 52:965–82. https://doi.org/10.1016/j.ijhydene.2023.08.293.

[44] Karabanova A, Berdiyeva P, van der Pal M, Johnsen RE, Deledda S, Blanchard D. Intrinsic kinetics in local modelling of thermochemical heat storage systems. Appl Therm Eng 2021;192:116880. https://doi.org/10.1016/j.applthermaleng.2021.116880.

[45] Jensen C, Duyar MS. Thermodynamic analysis of dry reforming of methane for valorization of landfill gas and natural gas. Energ Technol 2021;9(7):2100106. https://doi.org/10.1002/ente.202100106.

[46] Ginsburg JM, Piña J, El Solh T, de Lasa HI. Coke formation over a nickel catalyst under methane dry reforming conditions: thermodynamic and kinetic models. Ind Eng Chem Res 2005;44(14):4846–54. https://doi.org/10.1021/ie0496333.

[47] Nishimura A, Hayashi Y, Ito S, Kolhe ML. Performance analysis of hydrogen production for a solid oxide fuel cell system using a biogas dry reforming membrane reactor with Ni and Ni/Cr catalysts. Fuels 2023;4(3):295–313.

[48] Fu Q, Li Z, Liu Z, Wei W. Performance study of solid oxide fuel cell with Ni-foam indirect internal reformer: intrinsic reforming kinetics and temperature uniformity. Chem Eng J 2023;457:141170. https://doi.org/10.1016/j.cej.2022.141170.

[49] Marquardt T, Bode A, Kabelac S. Hydrogen production by methane decomposition: analysis of thermodynamic carbon properties and process evaluation. Energ Conver Manage 2020;221:113125. https://doi.org/10.1016/j.enconman.2020.113125.

[50] Subotić V, Harter P, Kusnezoff M, Napporn TW, Schroettner H, Hochenauer C. Identification of carbon deposition and its removal in solid oxide fuel cells by applying a non-conventional diagnostic tool. Sustainable Energy Fuels 2021;5(7): 2065–76. https://doi.org/10.1039/D0SE01914C.

[51] Evans JW. Introduction and the significance of electrometallurgy, reference module in materials science and materials engineering. Elsevier; 2016. 10.1016/B978-0-12-803581-8.03594-3.

[52] Dicks AL, Pointon KD, Siddle A. Intrinsic reaction kinetics of methane steam reforming on a nickel/zirconia anode. J Power Sources 2000;86(1):523–30. https://doi.org/10.1016/S0378-7753(99)00447-4.

[53] Tabish AN, Fan L, Farhat I, Irshad M, Abbas SZ. Computational fluid dynamics modeling of anode-supported solid oxide fuel cells using triple-phase boundary-based kinetics. J Power Sources 2021;513:230564. https://doi.org/10.1016/j.jpowsour.2021.230564.

[54] Unruean P, Plianwong T, Pruksawan S, Kitiyanan B, Ziff RM. Kinetic monte-carlo simulation of methane steam reforming over a nickel surface. Catalysts 2019;9(11): 946.

[55] Christov SG. Collision theory and statistical theory of chemical reactions. Berlin Heidelberg: Springer; 2012.

[56] Widom B. Collision theory of chemical reaction rates. Adv Chem Phys 1963: 353–86. https://doi.org/10.1002/9780470143513.ch8.

[57] Peleg M, Normand MD, Corradini MG. The arrhenius equation revisited. Crit Rev Food Sci Nutr 2012;52(9):830–51. https://doi.org/10.1080/10408398.2012.667460.

[58] Asadikiya M, Zhong Y. Oxygen ion mobility and conductivity prediction in cubic yttria-stabilized zirconia single crystals. J Mater Sci 2018;53(3):1699–709. https://doi.org/10.1007/s10853-017-1625-1.

[59] Guk E, Venkatesan V, Babar S, Jackson L, Kim J-S. Parameters and their impacts on the temperature distribution and thermal gradient of solid oxide fuel cell. Appl Energy 2019;241:164–73. https://doi.org/10.1016/j.apenergy.2019.03.034.

[60] Wang W-Y, Wang G-C. The first-principles-based microkinetic simulation of the dry reforming of methane over Ru(0001). Cat Sci Technol 2021;11(4):1395–406. https://doi.org/10.1039/D0CY01942A.

[61] Pham Minh D, Siang TJ, Vo D-V-N, Phan TS, Ridart C, Nzihou A. Chapter 4 - hydrogen production from biogas reforming: an overview of steam reforming, dry reforming, dual reforming, and tri-reforming of methane. In: Azzaro-Pantel C, editor. Hydrogen Supply Chains. Academic Press; 2018. p. 111–66. 10.1016/B978-0-12-811197-0.00004-X.

[62] Takahashi A, Inagaki R, Torimoto M, Hisai Y, Matsuda T, Ma Q, et al. Effects of metal cation doping in CeO2 support on catalytic methane steam reforming at low temperature in an electric field. RSC Adv 2020;10(25):14487–92. https://doi.org/10.1039/D0RA01721C.

[63] Agmon N. The grotthuss mechanism. Chem Phys Lett 1995;244(5):456–62. https://doi.org/10.1016/0009-2614(95)00905-J.

[64] Cai N, Zhou G, Müller K, Starr DE. Temperature and pressure dependent Mott potentials and their influence on self-limiting oxide film growth. Appl Phys Lett 2012;101(17). https://doi.org/10.1063/1.4764552.

[65] Tsuchiya M, Sankaranarayanan SKRS, Ramanathan S. Photon-assisted oxidation and oxide thin film synthesis: a review. Prog Mater Sci 2009;54(7):981–1057. https://doi.org/10.1016/j.pmatsci.2009.04.003.

[66] Pornprasertsuk R, Ramanarayanan P, Musgrave CB, Prinz FB. Predicting ionic conductivity of solid oxide fuel cell electrolyte from first principles. J Appl Phys 2005;98(10). https://doi.org/10.1063/1.2135889.

[67] Andersson M, Paradis H, Yuan J, Sundén B. Review of catalyst materials and catalytic steam reforming reactions in SOFC anodes. Int J Energy Res 2011;35(15): 1340–50. https://doi.org/10.1002/er.1875.

[68] Lima EC, Gomes AA, Tran HN. Comparison of the nonlinear and linear forms of the van't Hoff equation for calculation of adsorption thermodynamic parameters (ΔS° and ΔH°). J Mol Liq 2020;311:113315. https://doi.org/10.1016/j.molliq.2020.113315.

[69] Freund HJ, Messmer RP. On the bonding and reactivity of CO2 on metal surfaces. Surf Sci 1986;172(1):1–30. https://doi.org/10.1016/0039-6028(86)90580-7.